Journal of Molecular Liquids 313 (2020) 113492

Contents lists available at ScienceDirect

Journal of Molecular Liquids

journal homepage: www.elsevier.com/locate/molliq

# Analysis of transport processes in a reacting flow of hybrid nanofluid around a bluff-body embedded in porous media using artificial neural network and particle swarm optimization

Javad Mohebbi Najm Abad [a], Rasool Alizadeh [b], Abolfazl Fattahi [c], Mohammad Hossein Doranehgard [d], Ebrahim Alhajri [e], Nader Karimi [f,g,*]

[a] Department of Computer Engineering, Quchan Branch, Islamic Azad University, Quchan, Iran
[b] Department of Mechanical Engineering, Quchan Branch, Islamic Azad University, Quchan, Iran
[c] Department of Mechanical Engineering, University of Kashan, Kashan, Iran
[d] Department of Civil and Environmental Engineering, School of Mining and Petroleum Engineering, University of Alberta, Edmonton, Alberta T6G 1H9, Canada
[e] Department of Mechanical Engineering, Khalifah University, Abu Dahabi, United Arab Emirates
[f] School of Engineering and Materials Science, Queen Mary University of London, London E1 4NS, United Kingdom
[g] James Watt School of Engineering, University of Glasgow, Glasgow G12 8QQ, United Kingdom

ARTICLE INFO

*Article history:*
Received 6 May 2020
Received in revised form 26 May 2020
Accepted 30 May 2020
Available online 2 June 2020

*Keywords:*
Hybrid nanofluid
Artificial intelligence
Chemically reacting flow
Mixed convection
Predictor algorithms
Particle swarm optimization

ABSTRACT

This paper investigates heat and mass transfer in a hybrid nanofluid flow impinging upon a cylindrical bluff-body embedded in porous media and featuring homogenous and heterogeneous chemical reactions. The analysis includes mixed convection and local thermal non-equilibrium in the porous medium as well as Soret and Dufour effects. Assuming single-phase mixture, a laminar flow of $Al_2O_3$-Cu-water (Aluminium oxide-Copper-water) hybrid nanofluid is considered and coupled transport processes are simulated computationally. Due to the significant complexity of this problem, containing a large number of variables, conventional approaches to parametric study struggle to provide meaningful outcomes. As a remedy, the simulation data are fed into an artificial neural network to estimate the target responses. This shows that the volume fraction of nanoparticles, interfacial area of the porous medium and mixed convection parameter, are of primary importance. It is also observed that small variation in the volume fraction of nanoparticles can considerably alter the response of thermal and solutal domains. Further, it is shown that the parameters affecting the thermal process can modify the problem chemically. In particular, raising the volume fraction of nanoparticles enhances the production of chemical species. Furthermore, particle swarm optimization is applied to predict correlations for Nusselt and Sherwood numbers through a systematic identification of the most influential parameters. The current study clearly demonstrates the advantages of using the estimator algorithms to understand and predict the behaviours of complex thermo-chemical and solutal systems.



## 1. Introduction

The rapidly growing concerns on environmental pollutions and global warming [1,2], have motivated many attempts to improve the efficiency of transport processes. Utilizing various shapes of fins [3], ribs [4], turbulators and vortex generators [5] are some examples of these efforts. Further, blending nanoparticles with the base working fluid has been demonstrated to be an effective way of boosting thermal conductivity and results in improved heat transfer [6]. Many articles have appeared in recent years on the metallic, non-metallic and quasi-metallic nanoparticles (e.g. [7,8]) and the work in this area is ongoing. For years, nanofluids were manufactured of one type of nanoparticles. Applying the advantageous of different nanoparticles, recently, multiple kinds of nanoparticles have been simultaneously embedded in the base fluid. These nanofluids, regarded as hybrid nanofluid, feature higher thermal conductivity than those prepared by monotype nanoparticles [9]. Heat exchangers, heat pipes, chillers, solar heating and electrical chips are the instances of potential use of hybrid nanofluids [9,10].

Utilizing porous materials with high thermal conductivity is also a well demonstrated method of improving heat transfer. It has been already shown that combining porous media and nanofluids can enhance heat transfer considerably [11–14]. Some recent studies targeted increasing heat transfer by using porous media and hybrid nanofluids. Xiong el al. [15] numerically investigated free convection of hybrid nanofluid ($Fe_3O_4$ + MWCNT (Iron Oxide + Multi-walled carbon nanotubes)) in a

* Corresponding author at: School of Engineering and Materials Science, Queen Mary University of London, London E1 4NS, United Kingdom.
*E-mail address:* N.Karimi@qmul.ac.uk (N. Karimi).

https://doi.org/10.1016/j.molliq.2020.113492

**Nomenclature**

| | |
|---|---|
| $A_1, A_2, A_3, A_4, A_5$ | constants |
| $a$ | cylinder radius |
| $a_{sf}$ | interfacial area per unit volume of porous media |
| $Bi$ | Biot number $Bi = \frac{h_{sf} a_{sf}.a}{4k_f}$ |
| $c_1$ | concentration of species 1 |
| $c_2$ | concentration of species 2 |
| $C_p$ | specific heat at constant pressure |
| $C_s$ | concentration |
| $D$ | ratio of the diffusion coefficient |
| $D_1$ | solute diffusion coefficient of species 1 |
| $D_2$ | solute diffusion coefficient of species 2 |
| $Df$ | Dufour number $Df = \frac{D.k_f \quad C_\infty}{C_s.C_p(T_w - T_\infty}) \upsilon$ |
| $f(\eta)$ | radial velocity function |
| $f\ (\eta)$ | axial velocity function |
| $g$ | gravitational acceleration |
| $h$ | heat transfer coefficient |
| $h_{sf}$ | interstitial heat transfer coefficient |
| $k$ | thermal conductivity |
| $\bar{k}$ | freestream strain rate |
| $k_1$ | permeability of the porous medium |
| $k_m$ | mass transfer coefficient |
| $k_T$ | thermal diffusion ratio |
| $K_c$ | HOM parameter |
| $K_s$ | HET parameter |
| $m$ | shape factor |
| $N^*$ | ratio of concentration to thermal buoyancy forces $N^* = \frac{g.\beta_c.C_\infty}{4a\bar{k}^2}$ |
| $Nu$ | Nusselt number |
| $Nu_m$ | average Nusselt number |
| $p$ | fluid pressure |
| $P$ | non-dimensional fluid pressure |
| $P_0$ | the initial fluid pressure |
| $Pr$ | Prandtl number |
| $q_m$ | mass flux on the wall |
| $q_w$ | heat flux on the wall |
| $r$ | radial coordinate |
| $Re$ | freestream Reynolds number $Re = \frac{\bar{k}.a^2}{2\upsilon}$ |
| $S$ | interfacial area $S = \frac{a_{sf} D_1^{1/2}}{(\bar{k}\upsilon)}$ |
| $Sc$ | Schmidt number $Sc = \frac{\upsilon}{D}$ |
| $Sr$ | Soret number $Sr = \frac{D.k_f(T_w - T_\infty)}{T_\infty \quad C_\infty.\alpha}$ |
| $Sh$ | Sherwood number |
| $Sh_m$ | average Sherwood number |
| $T$ | temperature |
| $T_m$ | mean fluid temperature |
| $u, w$ | velocity components along $(r - z)$- axis |
| $z$ | axial coordinate |

*Greek symbols*

| | |
|---|---|
| $\alpha$ | thermal diffusivity |
| $\beta_C$ | coefficient of thermal expansion with concentration |
| $\beta_t$ | coefficient of thermal expansion |
| $\gamma$ | modified conductivity ratio $\gamma = \frac{k_f}{k_s}$ |
| $\gamma^*$ | Damköhler number $\gamma^* = \frac{k_R.a\ 1}{2D\ C_\infty}$ |
| $\eta$ | similarity variable, $\eta = \left(\frac{r}{a}\right)^2$ |
| $\theta(\eta)$ | non-dimensional temperature |
| $\lambda$ | permeability parameter, $\lambda = \frac{a^2}{4k_1}$ |
| $\lambda_1$ | dimensionless mixed convection parameter |
| $\varepsilon$ | porosity |
| $\mu$ | dynamic viscosity |
| $\upsilon$ | kinematic viscosity |
| $\rho$ | fluid density |
| $\phi_1, \phi_2$ | solid volume fraction of nanoparticles of nanoparticles 1 and 2. |

*Subscripts*

| | |
|---|---|
| $w$ | related to the external wall of the cylinder |
| $\infty$ | far field |
| $hnf$ | hybrid nanofluid |
| $nf$ | nanofluid |
| $f$ | fluid |
| $s$ | solid |

porous enclosure under magnetic effects. It was shown that variation of Reynolds and Darcy number as well as thermal radiation were in the same direction of Nusselt number, while Hartmann number renders an adverse effect. Natural convection of $Al_2O_3$-Cu water hybrid nanofluid in a differentially heated porous cavity was studied by Mehryan et al. [16]. It was found that heat transfer enhancement by increasing nanofluid volume fraction might be completely suppressed by applying certain kinds of porous materials.

Sajjadi et al. [17] numerically simulated MHD (Magneto Hydro Dynamics) natural convection of MWCNT–$Fe_3O_4$/water hybrid nanofluid in a porous cavity. The existence of magnetic field could smear the influence of Rayleigh number on heat transfer, while adding the hybrid nanofluid to the base fluid augments the role of Rayleigh number. Free convection of hybrid nanoparticles of MWCNT and $Fe_3O_4$ in water in a porous circle sector was investigated by Manh et al. [18]. They presented a correlation for mean Nusselt number as a function of Hartmann, Rayleigh and Darcy number. Natural convection of hybrid nanofluid of MWCNT-$Fe_3O_4$-water in an enclosure filled with a two-layer porous media was conducted by Mehryan et al. [19]. Heat transfer was augmented at lower values of solid-liquid interface convection parameter and higher values of porosity ratio. This study considered the local thermal non-equilibrium assumption for calculating the temperature field within the porous medium. Similarly, Alizadeh et al. [20] showed the critical effect of the non-equilibrium assumption on the thermal mode of the system through numerical simulation of an external hybrid nanofluid flow over a cylinder surrounded by porous materials.

Jerry et al. [21] studied mixed convection of Ag-MgO (Silver -Magnesium oxide) hybrid nanoparticles in water through a horizontal rectangular porous channel. The variations of thermal and hydrodynamic parameters in the temporal domain were scrutinized. The heat transfer and fluid flow were characterized by a pattern in spatial and temporal domain. Darcy number determined the thermal response of the system; at low Darcy numbers, heat transfer showed a single-maximum trend, while it had a monotonic increasing trend at high values of Darcy number. The forced convection of $Al_2O_3$–CuO–water hybrid nanofluid in a cylinder filled with porous medium was conducted by Aminian et al. [22]. These authors reported that declining Darcy number intensifies the heat transfer rate, while it poses an adverse effect on the pressure drop.

The fluid flow near a stagnation zone is called stagnation-point flow [23]. This kind of flow usually occurs on the solid surface of the bluff bodies [24] and has been widely applied in aerospace technologies and cooling of electronics [23]. Stagnation-point flows over a permeable stretching sheet in a nanofluid flow [25], porous medium [26–28] and by considering radiation and mixed convection heat transfer [24] have been already studied. Recently, a stagnation point flow over a stretching-shrinking surface merging in a hybrid nanofluid has been conducted [29]. The Joule heating was assumed

to be active owing to electrical conductivity of the base fluid. It was shown that increases in Eckert number improved the thermal characteristic of hybrid nanofluid.

The current problem includes stagnation-point hybrid nanofluid flow over a bluff body embedded in a porous media that further includes surface chemical reactions. The large number of influencing parameters render heat and mass transfer predictions too laborious. This is due to many interconnections amongst the parameters and the complex physics of the problem. Therefore, a predictive tool having the capability of capturing the nonlinear and complex underlying physics with a high degree of accuracy is highly desirable. Comparing to the other similar algorithms, the artificial neural network (ANN) is the most capable of learning and estimating complex and non-linear problems, widely encountered in the engineering [30]. Given the powerful data-driven, self-adaptive and flexible features of a machine learning [31], ANN is employed in this study. This method has been already utilized to understand the responses of thermal systems with respect to pertinent variables. Abdollahi et al. [32] used ANN to find the optimum hydrothermal working point of a grooved channel filled with a hybrid nanofluid and equipped with reflectors in the laminar regime. Similar work was performed in a vortex-generator channel involving hybrid nanofluid using multi-objective genetic algorithm by Abdollahi and Shams [33]. The results of numerical simulation of Eulerian-Lagrangian approach were used to train the model. Prediction of entropy generation of Ag-MgO-water hybrid nanofluid in a mini-channel was also carried out using ANN [34]. Bagheri et al. [35] predicted Nusselt number in a C-shaped cavity occupied with a hybrid nanofluid by means of ANN.

The numerical simulation of Cu-$Al_2O_3$-water hybrid nanofluid following over a cylinder in a porous domain is conducted in this work. Mixed convection as well as homogenous and heterogeneous chemical reactions are considered. To capture the heat transfer caused by mass diffusion and vice versa, Dufour and Soret effects are further considered. The current study evaluates the ability of the machine-learning methods to predict the behavior of a problem with many interconnected parameters. It is requires choosing the algorithms with reasonable errors in their predictions. Therefore, the numerical results are applied to train the ANN, leading to prediction of the targeted parameters in a wide range. Further, particle swarm optimization (PSO) method is applied to precisely extract correlations for Nusselt and Sherwood numbers [36,37].

## 2. Physical description of the problem and mathematical formulation

Fig. 1 shows the geometry and physical domain of the current problem. The nanofluid passes over an infinitely long cylinder embedded in a porous medium and develops a stagnation-point flow. The flow includes heterogeneous and homogenous chemical reactions. The following assumptions are made throughout this work.

- The nanofluid flow is steady and laminar.
- The nanofluid is assumed to be Newtonian and single phase [38–41].
- The cylinder is assumed to be infinitely long, and the porous medium is homogenous, isotropic and under local thermal non-equilibrium.
- The viscous dissipation of kinetic energy of the flow is ignored. Also, porosity, specific heat, density and thermal conductivity are assumed to be constant and thus the thermal dispersion effects are ignored.
- A moderate range of pore-scale Reynolds number is considered in the porous medium and hence non-linear effects in momentum transfer are deemed to be negligibly small.

The continuity of mass, radial and axial direction of momentum and energy equations are written respectively as follows.

$$\frac{\partial u}{\partial r}+\frac{u}{r}+\frac{\partial w}{\partial z}=0 \tag{1}$$

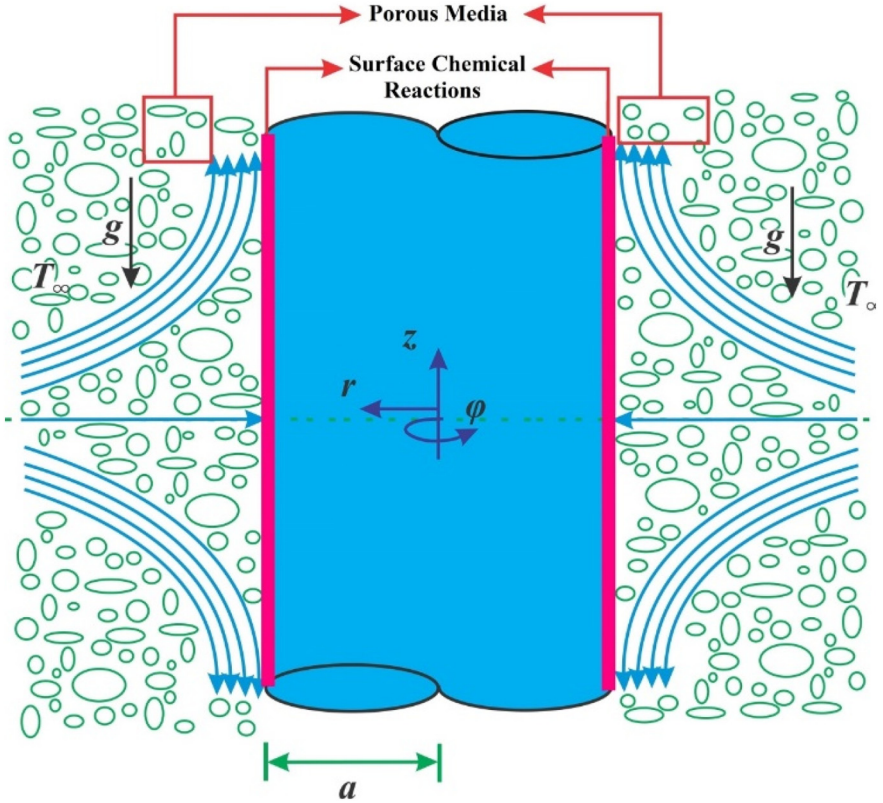


**Fig. 1.** Schematic configuration of bluff-body under radial impinging flow surrounded by porous media.

$$\frac{\rho_{hnf}}{\varepsilon^2}\left(u\frac{\partial u}{\partial r}+w\frac{\partial u}{\partial z}\right)=-\frac{\partial p}{\partial r}+\frac{\mu_{hnf}}{\varepsilon}\left(\frac{\partial^2 u}{\partial r^2}+\frac{1}{r}\frac{\partial u}{\partial r}-\frac{u}{r^2}+\frac{\partial^2 u}{\partial z^2}\right)-\frac{\mu_{hnf}}{k_1}u, \quad (2)$$

$$\begin{aligned}\frac{\rho_{hnf}}{\varepsilon^2}\left(u\frac{\partial w}{\partial r}+w\frac{\partial w}{\partial z}\right)&=-\frac{\partial p}{\partial z}\\&+\frac{\mu_{hnf}}{\varepsilon}\left(\frac{\partial^2 w}{\partial r^2}+\frac{1}{r}\frac{\partial w}{\partial r}+\frac{\partial^2 w}{\partial z^2}\right)\mp g.(\rho.\beta_t)_{hnf}\left[T_f-T_\infty\right]\\&+g.(\rho.\beta_c)_{hnf}[c_2-c_\infty]-\frac{\mu_{hnf}}{k_1}w,\end{aligned} \quad (3)$$

$$\begin{aligned}u\frac{\partial T_f}{\partial r}+w\frac{\partial T_f}{\partial z}&=\alpha_{hnf}\left(\frac{\partial^2 T_f}{\partial r^2}+\frac{1}{r}\frac{\partial T_f}{\partial r}+\frac{\partial^2 T_f}{\partial z^2}\right)\\&+\frac{h_{sf}.a_{sf}}{(\rho.C_p)_{hnf}}(T_s-T_f)+\frac{D_2\,k_T}{C_{p_s}.C_{p\,hnf}}\left[\frac{\partial^2 c_2}{\partial r^2}+\frac{1}{r}\frac{\partial c_2}{\partial r}+\frac{\partial^2 c_2}{\partial z^2}\right],\end{aligned} \quad (4)$$

where all parameters defined in the nomenclature.

The energy Eq. (4) contains the Dufour effect [42,43] by the last term on the right hand side. Further, the heat transfer within the solid phase of the porous medium can be expressed by

$$k_s\left(\frac{\partial^2 T_s}{\partial r^2}+\frac{1}{r}\frac{\partial T_s}{\partial r}+\frac{\partial^2 T_s}{\partial z^2}\right)-h_{sf}.a_{sf}(T_s-T_f)=0, \quad (5)$$

in which $k_s$ and $T_s$ are thermal conductivity and temperature of the solid porous medium. Considering homogenous-heterogeneous (HOM-HET) reactions, mass transfer of chemical species is presented by an advective-diffusive model, as the following [44].

$$u\frac{\partial c_1}{\partial r}+w\frac{\partial c_1}{\partial z}=D_1\left(\frac{\partial^2 c_1}{\partial r^2}+\frac{1}{r}\frac{\partial c_1}{\partial r}+\frac{\partial^2 c_1}{\partial z^2}\right)-k_c c_1 c_2^2-a_{sf}.k_s.c_1, \quad (6)$$

$$\begin{aligned}u\frac{\partial c_2}{\partial r}+w\frac{\partial c_2}{\partial z}&=D_2\left(\frac{\partial^2 c_2}{\partial r^2}+\frac{1}{r}\frac{\partial c_2}{\partial r}+\frac{\partial^2 c_2}{\partial z^2}\right)\\&+\frac{D_2\,k_T}{T_m}\left(\frac{\partial^2 T_f}{\partial r^2}+\frac{1}{r}\frac{\partial T_f}{\partial r}+\frac{\partial^2 T_f}{\partial z^2}\right)+k_c c_1 c_2^2+a_{sf}.k_s.c_1.\end{aligned} \quad (7)$$

The mass transfer Eqs. (6) and (7) involve the classical Fickian diffusion as well as solute diffusion by means of thermal gradient, called Soret effect, which is the second bracketed term on the right hand side of Eq. (7) [45,46]. In Eqs. (3)–(7) the subscript "f" refers to the fluid properties. Further, $D_1$ and $D_2$ indicate molecular diffusion coefficient of species 1 and 2, having respectively the concentration of $c_1$ and $c_2$. $k_s$ and $k_c$ are the HET and HOM reaction rate constant, correspondingly. The HOM-HET reactions used in the current study are respectively defined as

$$S2+2S1\rightarrow 3S1, \quad (8)$$

$$S2\rightarrow S1, \quad (9)$$

where $S1$ and $S2$ are the species 1 and 2. The HOM reaction rate for is given by [44]

$$\frac{\partial c_1}{\partial t}=\frac{\partial c_2}{\partial t}=-k_c c_2 {c_1}^2. \quad (10)$$

The HET reaction rate performing on the fluid-solid interface of the cylinder surface is represented by [47]

$$r_p=-k_s\,a_{sf}c_2. \quad (11)$$

The HET reaction rate then can be related to the solute gradient as [44]

$$D_1\frac{\partial c_1}{\partial n}=-D_2\frac{\partial c_2}{\partial n}=k_s c_2, \quad (12)$$

in which $n$ is the normal direction towards the fluid.

The hydrodynamic boundary conditions can be written as

$$r=a: w=0, u=0, \quad (13)$$

$$r=\infty: w=2\bar{k}z, u=-\bar{k}\left(r-\frac{a^2}{r}\right). \quad (14)$$

Eq. (13) demonstrates the no-slip boundary conditions over the cylinder walls, with radius $a$. Also, Eq. (19) shows that analogous to the Hiemenz flow, the current viscous flow approaches the potential flow in the limit of $r\rightarrow\infty$[48–50].

The thermal boundary conditions give

$$\begin{aligned}r=a:\quad &T_f=T_w=\text{Constant},\\&T_s=T_w=\text{Constant},\\r=a:\quad &T_f=T_\infty,\\&T_s=T_\infty,\end{aligned} \quad (15)$$

in which $T_w$ and $T_\infty$ indicate the cylinder surface and the free-stream temperature, respectively.

The solute transport boundary conditions are given by

$$r=a:\frac{\partial C_1}{\partial r}=+\frac{k_3}{D_1}C_1,\frac{\partial C_2}{\partial r}=-\frac{k_3}{D_2}C_2, r\rightarrow\infty: C_1\rightarrow C_2 C_2\rightarrow 0 \quad (16)$$

$c_\infty$ is the concentration at the free-stream limit.

## 3. Self-similar solution of the governing equations

Applying the following similarity transformation, Eqs. (1) to (7) are reduced to the forms that can be solved more conveniently.

$$u=-\frac{\bar{k}.a}{\sqrt{\eta}}f(\eta), w=\left[2\bar{k}f'(\eta)\right]z, p=\rho_f\bar{k}^2a^2P, \quad (17)$$

where $\eta=\left(\frac{r}{a}\right)^2$ is the non-dimensional radial variable. Some algebraic manipulations reveals the following non-dimensional form.

$$\begin{aligned}&\varepsilon.[\,\eta f'''+f'']+A_1.A_2.\,Re\left[1+ff''-(\,f')^2\right]\\&+\varepsilon^2.\lambda[1-f']\mp\varepsilon^2.A_1.A_6.\,Re.\lambda_1\theta_f+\varepsilon^2.A_1.\,Re.N^*.[C_2-1]\\&=0,\end{aligned} \quad (18)$$

$$P-P_0=-\frac{A_2}{2\varepsilon^2}\left(\frac{f^2}{\eta}\right)-\frac{1}{A_1.\varepsilon}\left[\left(\frac{f'}{Re}\right)+\frac{\lambda}{A_1.\,Re}\int_1^\eta\frac{f}{\eta}d\eta\right]-2\left[\frac{A_2}{\varepsilon^2}+\frac{\lambda}{A_1.\,Re}\right]\left(\frac{z}{a}\right)^2, \quad (19)$$

in which $Re=\frac{\bar{k}.a^2}{2\upsilon_f}$ depicts the Reynolds number of freestream, $\lambda=\frac{a^2}{4k_1}$ is the permeability parameter, $\lambda_1=\frac{Gr}{Re^2}=\frac{g.\beta_t(T_w-T_\infty)}{4a\bar{k}^2}$ denotes the dimensionless mixed convection parameter , $N^*=\frac{g.\beta_c.C_\infty}{4a\bar{k}^2}$ ratio of concentration to thermal buoyancy forces and prime symbol indicates the derivative against $\eta$. The constant $A_1$ and $A_2$ are defined as

$$A_1=(1-\phi_1)^{2.5}(1-\phi_2)^{2.5},$$

$$A_2=(1-\phi_2)\left[(1-\phi_1)+\phi_1\left(\frac{\rho_{s_1}}{\rho_f}\right)\right]+\phi_2\left(\frac{\rho_{s_2}}{\rho_f}\right).$$

Considering Eqs. (13), (14) and (17), the boundary conditions for Eqs. (18) and (19) are given by

$$\eta = 1 : f'(1) = 0, f(1) = 0, \tag{20a}$$

$$\eta \to \infty : f'(\infty) = 1. \tag{20b}$$

Taking the following transformation,

$$\theta_f(\eta) = \frac{T_f(\eta) - T_\infty}{T_w - T_\infty}, \tag{21}$$

the energy Eq. (4) is turned into non-dimensional form, which yields

$$A_4.A_5\left[\eta\theta''_f + \theta'_f\right] + Re.\ Pr.A_3.A_5\left(f.\theta'_f\right) + Bi.A_5\left(\theta_s - \theta_f\right) + Df.\ Pr.A_3.D\left[\eta C''_2 + C'_2\right] = 0, \tag{22}$$

in which $Bi = \frac{h_{sf}a_{sf}.a}{4k_f}$ represents the Biot number and $Df = \frac{D_1.k_T}{C_s.C_{pf}}\frac{c_\infty}{(T_w - T_\infty)\upsilon_f}$ is the Dufour number. The constants $A_3$ to $A_5$ in Eq. (22) are defined by

$$A_3 = (1-\phi_2)\left[(1-\phi_1) + \phi_1\frac{(\rho.C_p)_{s_1}}{(\rho.C_p)_f}\right] + \phi_2\frac{(\rho.C_p)_{s_2}}{(\rho.C_p)_f},$$

$$A_4 = \frac{k_{s_1} + (s-1)k_f - (s-1)\phi_1(k_f - k_{s_1})}{k_{s_1} + (s-1)k_f + \phi_1(k_f - k_{s_1})}.\frac{k_{s_2} + (s-1)k_{bf} - (s-1)\phi_2(k_{bf} - k_{s_2})}{k_{s_2} + (s-1)k_{bf} + \phi_2(k_{bf} - k_{s_2})},$$

$$A_5 = (1-\phi_2)\left[(1-\phi_1) + \phi_1\frac{C_{p_{s_1}}}{C_{p_f}}\right] + \phi_2\frac{C_{p_{s_2}}}{C_{p_f}}. \tag{23}$$

The thermal boundary conditions subsequently reduce to

$$\eta = 1 : \theta_f(1) = 1 \tag{24a}$$

$$\eta \to \infty : \theta_f(\infty) = 0. \tag{24b}$$

Substitution of Eq. (21) into Eq. (5), the energy equation for the solid porous media takes the form of

$$\eta\theta''_s + \theta'_s - Bi.\gamma\left(\theta_s - \theta_f\right) = 0, \tag{25}$$

with the boundary conditions as follows.

$$\eta = 1 : \quad \theta_s(1) = 1$$
$$\eta \to \infty : \quad \theta_s(\infty) = 0. \tag{26}$$

In Eq. (25), $\gamma = \frac{k_f}{k_s}$ is the modified conductivity ratio. Aiding Eq. (21) and the definition of

$$C(\eta) = \frac{c(\eta)}{c_\infty}, \tag{27}$$

the mass transport Eqs. (6) and (7) are transformed into dimensionless forms of

$$Pr\left[\eta C''_1 + C'_1\right] + Re.\ Pr.Sc\left[f.C'_1 - K_c.C_1.C_2^2 - K_s.S.C_1\right] = 0, \tag{28a}$$

$$Pr.D.\left[\eta C''_2 + C'_2\right] + Sr.Sc.D.\left[\eta\theta''_f + \theta'_f\right] + Re.\ Pr.Sc\left[f.C'_2 + K_c.C_1.C_2^2 + K_s.S.C_1\right] = 0, \tag{28b}$$

in which, $Sc = \frac{\upsilon_f}{D_1}$ and $Sr = \frac{D_1.k_T(T_w - T_\infty)}{T_m\ c_\infty.\alpha_f}$ describes Schmidt and Soret number, respectively. Further, $K_c = \frac{k_c c_\infty^2}{\bar{k}}$ and $K_s = \frac{k_s\upsilon^{1/2}}{D\bar{k}^{1/2}}$ denote correspondingly the non-dimensional HOM and HET parameter, in which $\upsilon$ is dynamic viscosity of the nanofluid. $S = \frac{a_{sf}D_1{}^{1/2}}{(\bar{k}\upsilon)}$ is the non-dimensional interfacial area of the porous medium. The mass transfer equations are closed by the following boundary conditions.

$$\eta = 1 : \quad C'_1(1) = +\gamma^* C_1(1)$$
$$C'_2(1) = -\frac{\gamma^*}{D}C_2(1),$$
$$\eta \to \infty : \quad C_1(\infty) = 1$$
$$C_2(\infty) = 0, \tag{29b}$$

where $\gamma^* = \frac{k_3.a}{2D_1}$ indicates Damköhler number.

The numerical procedure aims to solve Eqs. (18), (22), (25), (28a) and (28b) along with the boundary conditions of Eqs. (20a), (20b), (24a), (24b), (26), (29a) and (29b) using an implicit, iterative finite-difference method [28]. One of the important non-dimensional parameters to understand the thermal performance of the current problem is the Nusselt number, *Nu*, which should be calculated using the definition of the convection heat transfer coefficient, *h*:

$$h = \frac{q_w}{T_w - T_\infty} = \frac{-k_{hnf}\left(\frac{\partial T_f}{\partial r}\right)_{r=a}}{T_w - T_\infty} = -\frac{2k_{hnf}}{a}\frac{\partial\theta_f(1)}{\partial\eta}, \tag{30}$$

and

$$q_w = -\frac{2k_{hnf}}{a}\frac{\partial\theta_f(1)}{\partial\eta}T_w - T_\infty, \tag{31}$$

$$Nu = \frac{h.a}{2k_f} = -\frac{k_{hnf}}{k_f}\theta'_f(1) = -A_4.\theta'_f(1). \tag{32}$$

Also, the coefficients of mass transfer and mass transfer rate are given by

$$k_m = \frac{q_m}{C_\infty} = \frac{-D_1\left(\frac{\partial c_1}{\partial r}\right)_{r=a}}{c_\infty} = -\frac{2D_1}{a}\frac{\partial C_1(1)}{\partial\eta}, \tag{33}$$

where $q_m$ is the mass flow rate at the cylinder wall, which is

$$q_m = -\frac{2D_1}{a}\frac{\partial C_1(1)}{\partial\eta}C_w - C_\infty. \tag{34}$$

Hence, Sherwood number is given by

$$Sh = \frac{k_m.a}{2D_1} = -C'_1(\eta = 1). \tag{35}$$

## 4. Hybrid nanofluid characterization

The hybrid nanofluid is made of $Al_2O_3$ and Cu nanoparticles suspended in water as the base fluid. The volume fractions of the $Al_2O_3$ and Cu nanoparticles are denoted by $\phi_1$ and $\phi_2$, respectively. The hybrid nanofluid is assumed to be a mixture of various volume fractions of Cu nanoparticles into the $Al_2O_3$-water nanofluid with fixed value of $\phi_1 = 0.1\%$. Therefore, in the current study, only the volume fraction of the Cu nanoparticles, $\phi_2$, is varied [51–53]. The determining equations for thermo-physical properties of the hybrid nanofluid of Cu-$Al_2O_3$-water are depicted in Table 1. Owing to the precision of its thermo-physical correlations [54], this type of hybrid nanofluid is chosen in this study.

Thermal conductivity of the hybrid nanofluid in Table 1 includes a shape factor parameter, *m*, which is set to 3 for the spherical nanoparticles

**Table 1**
Equations for thermo-physical properties of the hybrid nanofluid [54].

| Properties | Hybrid nanofluid |
|---|---|
| Density | $\rho_{hnf}=\rho_f(1-\phi_2)\left[(1-\phi_1)+\phi_1\left(\frac{\rho_{s_1}}{\rho_f}\right)\right]+\phi_2\rho_{s_2}$ |
| Heat capacity | $(\rho.C_p)_{hnf}=(\rho.C_p)_f(1-\phi_2)\left[(1-\phi_1)+\phi_1\frac{(\rho.C_p)_{s_1}}{(\rho.C_p)_f}\right]+\phi_2(\rho.C_p)_{s_2}$ |
| Viscosity | $\mu_{hnf}=\frac{\mu_f}{(1-\phi_1)^{2.5}(1-\phi_2)^{2.5}}$ |
| Thermal conductivity | $\frac{k_{hnf}}{k_{bf}}=\frac{k_{s_2}+(m-1)k_{bf}-(m-1)\phi_2(k_{bf}-k_{s_2})}{k_{s_2}+(m-1)k_{bf}+\phi_2(k_{bf}-k_{s_2})}$ <br> $\frac{k_{bf}}{k_f}=\frac{k_{s_1}+(m-1)k_f-(m-1)\phi_1(k_f-k_{s_1})}{k_{s_1}+(m-1)k_f+\phi_1(k_f-k_{s_1})}$ |

[54]. The thermo-physical properties of the basic components of the hybrid nanofluid are presented in Table 2 for the standard temperature of 25 ° C.

## 5. Validation and grid independency

To demonstrate independency of the results from the grid size, as well as precision of the numerical procedure, various cell numbers were compared. To do so, the surface averaged values of Nusselt and Sherwood numbers were calculated for mesh sizes of 51 × 18, 102 × 36, 204 × 72, 408 × 144 and 816 × 288. Table 3 shows there is no considerable difference between the parameters computed on the grid size of 408 × 144 and those of finer grids. Therefore, the grid size of 408 × 144 was chosen for meshing the $\eta-\varphi$ plane. It should be pointed out that the grid features a non-uniform structure in the normal direction to the cylinder, $\eta$, to capture the sharp gradient of the parameters, while it is uniformly sized in the other direction.

Tables 4 and 5 show that if the porosity approaches unity indicating no porous material, the current numerical results reduce to those reported by Wang [56] and Gorla [57] on impinging flow over a cylinder. Also, it was verified that for large values of Biot number, the current results under the assumption of local thermal non-equilibrium reproduce to the local thermal equilibrium results reported in Ref. [27].

The numerical procedure was terminated when the difference between the two subsequent residuals of each discretised equation become less than $10^{-7}$. Due to its superior stability, Crank-Nicolson second-order method was applied to discretize the governing equations through a finite difference method [58]. The temporal term was also discretized using backward second-order scheme [28]. The second-order discretization provides higher accuracy in transforming differential to algebraic equations involved in this study.

**Table 2**
Thermo-physical properties of the components of the hybrid nanofluid [55].

| Properties | Water | $Al_2O_3$ | Cu |
|---|---|---|---|
| $\rho\left(\frac{kg}{m^3}\right)$ | 997.0 | 3970 | 8933 |
| $C_p\left(\frac{J}{kg.K}\right)$ | 4180 | 765 | 385 |
| $k\left(\frac{W}{m.K}\right)$ | 0.6071 | 40 | 400 |

**Table 3**
Grid independence test at $Df=1.0$, $Bi=0.1$, $Sr=0.5$, $Re=5.0$, $\lambda=10$, $Sc=0.1$.

| Mesh size | $Nu_m$ | $Sh_m$ |
|---|---|---|
| 51 × 18 | 1.540873 | 0.588014 |
| 102 × 36 | 1.499256 | 0.555648 |
| 204 × 72 | 1.479155 | 0.527381 |
| 408 × 144 | 1.465920 | 0.467275 |
| 816 × 288 | 1.465773 | 0.468014 |

**Table 4**
A comparison of the current simulation results and those of Ref. [56] for unity porosity and very large permeability for $Re=10$ and 1.0.

| η | $Re=1.0$ | | | | $Re=10$ | | | |
|---|---|---|---|---|---|---|---|---|
| | Ref. [56] | | Current results | | Ref. [56] | | Current results | |
| | $f$ | $\acute{f}$ | $f$ | $\acute{f}$ | $f$ | $\acute{f}$ | $f$ | $\acute{f}$ |
| 1.2 | 0.02667 | 0.25302 | 0.02693 | 0.25993 | 0.06638 | 0.58982 | 0.06631 | 0.06610 |
| 1.4 | 0.09665 | 0.43724 | 0.09652 | 0.43710 | 0.21400 | 0.84821 | 0.21393 | 0.21379 |
| 1.6 | 0.19836 | 0.57315 | 0.19828 | 0.57329 | 0.39532 | 0.94852 | 0.39541 | 0.39535 |
| 1.8 | 0.32361 | 0.67444 | 0.32365 | 0.67438 | 0.58919 | 0.98380 | 0.58914 | 0.58926 |
| 2.0 | 0.46674 | 0.75054 | 0.46683 | 0.75046 | 0.78731 | 0.99522 | 0.78735 | 0.78729 |

## 6. Estimator and optimizer algorithms

### 6.1. Feedforward artificial neural network: Multi-Layer Perceptron (MLP)

Artificial neural network is an optimizer and estimator tool, inspired by the biological neural networks that constitute animal brains [59]. ANN requires learning to do expected tasks by providing the examples of the system. ANN does not need to include programming of task-specific rules. It is structured based on the connected units, called artificial neurons, playing similar to biological neural units [60]. In this paper, MLP neural network is used to estimate the output parameters. The structure of this network typically includes three layers, consisting of an input layer, a hidden layer, and an output layer. An input signal transmits to the neurons, showed by balls in Fig. 2, through connections, which are segment lines in this figure, and can be adjusted by the weight implemented on each connection.

If the model has $n$ input(s) then the input layer contains $n+1$ neurons. The first neuron, with a value of 1, is biased and the other neurons receive input data. The number of neurons in the second layer, called the hidden layer, is $m+1$. The appropriate value for $m$ can be calculated at the time of network creation by performing multiple tests. In this layer, similar to the first layer, one neuron plays the bias role. Other neurons apply an activation function to the sum of the weighted output of the previous layer that is [60]

$$f_i=g\left(w_{0,i}+\sum_{j=1}^{n}w_{j,i}\,x_j\right), \tag{36}$$

in which, $w_{0,i}$ is the weight between the bias and the $i$-th neuron of the hidden layer. Also, $w_{j,i}$ is the weight between the $j$-th neuron of the input layer and $i$-th neuron of the hidden layer. Furthermore, $x_j$ and $f_i$ shows the $j$-th input of the neural network and the output of $i$-th neuron of the hidden layer, respectively. For $g$ as an activation function, a variety of functions such as logistic, hyperbolic and exponential can be used.

**Table 5**
A comparison of the present numerical results and those of Ref. [57] for unity porosity and very large permeability for various Reynolds numbers.

| $Re$ | $\theta$ | |
|---|---|---|
| | Ref. [57] | Current results |
| 0.01 | 0.84549 | 0.84557 |
| 0.1 | 0.73715 | 0.73701 |
| 1.0 | 0.46070 | 0.46045 |
| 10 | 0.02970 | 0.02983 |

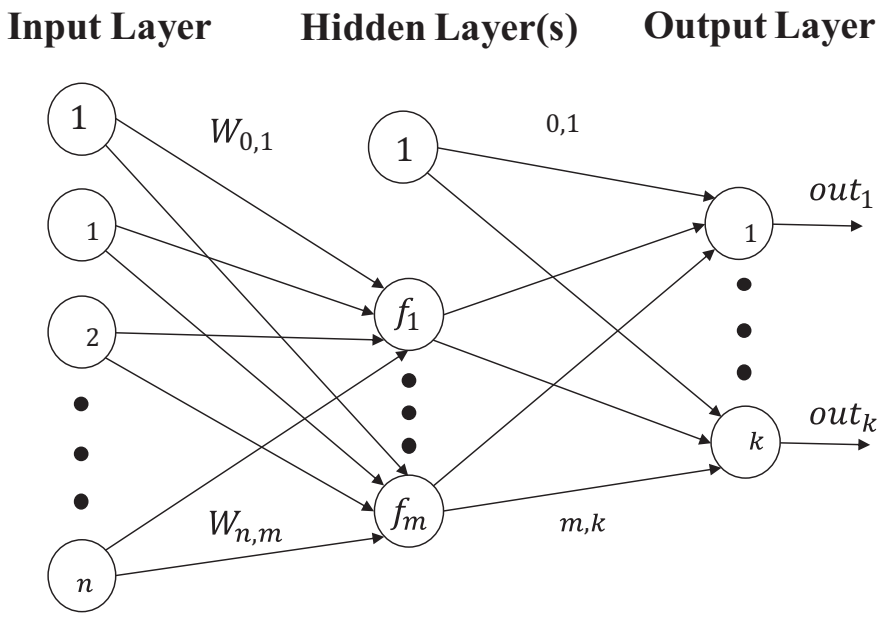


**Fig. 2.** The schematic view of a typical artificial neural network with three layers.

Similar to the hidden layer, each neuron of the output layer also applies the activation function to the sum of the weighted output of its predecessor layer as follows [60].

$$Out_i = h\left(v_{0,i} + \sum_{j=1}^{m} v_{j,i} f_j\right), \tag{37}$$

where $v_{0,i}$ and $v_{j,i}$ are the weights between the bias and the $j$-th neuron of the hidden layer and the latter with $i$-th neuron of the output layer, respectively.

Usually, the neural network training is performed using the error propagation algorithm. This process learns the weights between the network layers through supervised learning. The learning error rate is calculated from the difference between the neural network outputs and the expected ones in the training dataset. It should be noted that the configuration of the MLP network has a significant impact on its performance. Typically, to reduce the error rate, the appropriate network configuration is determined by repeated testing of the various choices. For this purpose, the number of neurons of hidden layer, and the activation function of the neurons in the hidden and output layer are determined by various experiments. In these experiments, different values are considered for these parameters and the error value of the model is calculated.

*6.1.1. Feature selection based on mutual information*

Selecting useful features has been a challenge in system identification problems. There are various methods to select the appropriate inputs based on the correlation between the data and the model output. This choice can be made by maximizing the statistical dependency criterion on the model output and minimizing the Mutual Information (MI) amongst the set of selected features. This is an applicable way to relate feature subset to output vector. MI is calculated between two features of $x$ and $y$ with the following equation.

$$I(x;y) = \iint p(x,y)\ \log\frac{p(x)}{p(x)p(y)}dxdy, \tag{38}$$

in which $p(x)$, $p(y)$ and $p(x,y)$, respectively, are the probability density functions of the variables $x$, $y$, and their simultaneous occurrence.

In order to minimize the overall error of any models, maximal dependence to the model output is essentially required. For this purpose, an algorithm as Minimum redundancy maximum relevance (MRMR) is applied to select the set of features in order to obtain the maximum correlation with the model output and the minimum correlation between the input features. In fact, the max-relevance set of features may contain features with high mutual correlations. If two features have the same aspects of the target class in the same way, there will be no benefit in having both of them as the members of the selected features set. The time complexity of the MRMR algorithm is exponential. It means that it is required to calculate exponentially increasing mathematical operations for retrieving a long list of parameters. For this reason, some methods, such as F-test correlation difference (FCD) and Mutual Information Difference (MID) have been proposed to approximate it. The recent experiments, however, show the interests of MID in non-linear problem [61]. The MID is computed as the following [62].

$$MID = \max_{i\in\varphi(S)}\left[I(i,h) - \frac{1}{|S_f|}\sum_{j\in S} I(i,j)\right], \tag{39}$$

where $S_f$ is the set of selected features. The advantage of using *MID* is that although it has an acceptable estimation of MRMR, its computational complexity is low. In other words, low overhead, high speed and reliability have led to the use of *MID* to select suitable features.

*6.2. Particle Swarm Optimization (PSO)*

The PSO algorithm is one of the most important intelligent optimization algorithms that fall into the field of swarm intelligence. This algorithm is inspired by the social behavior of the swarm of birds and fish [63]. It starts by collecting random solutions and then generating updates to search for the optimal solution. In each iteration, each particle is updated with two "best" values. The first is the best solution the particle has ever obtained in its movement. This is called the *pbest* value. Another "best" is the value so far earned by every single particle in the population. This is the best global value and is called *gbest*.

The particles move around the search space to find the best solution. For this purpose, in each iteration, the particle's velocity is separately calculated for all of them using the following equation [64].

$$v_i(t+1) = wv_i(t) + c_1r_1[pbest(t) - x_i(t)] + c_2r_2[gbest(t) - x_i(t)]. \tag{40}$$

**Table 6**
Ordering of feature prioritization for Nusselt number.

| Order | 1 | 2 | 3 | 4 | 5 | 6 | 7 | 8 | 9 | 10 | 11 | 12 | 13 | 14 | 15 | 16 |
|---|---|---|---|---|---|---|---|---|---|---|---|---|---|---|---|---|
| Feature | *Re* | $\lambda_1$ | $\phi_2$ | *Pr* | $\gamma^*$ | *D* | $N^*$ | *Df* | *S* | $\lambda$ | $K_c$ | *Bi* | *Sr* | $\gamma$ | *Sc* | $K_s$ |

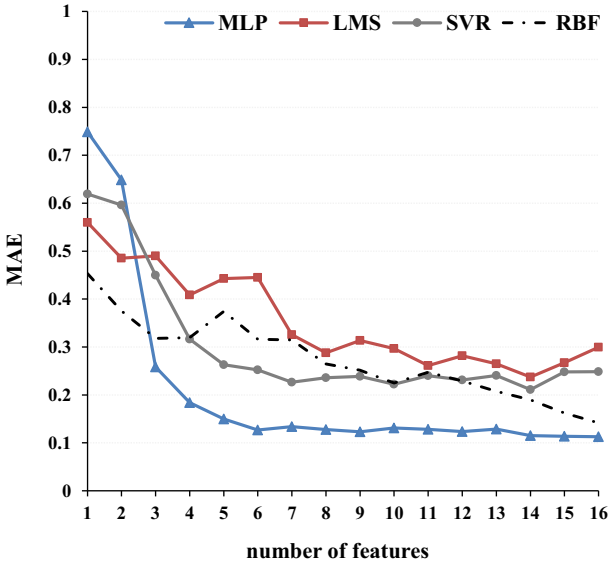


**Fig. 3.** Mean absolute error (MAE) to estimate Nusselt number for various potential models.

In Eq. (40), *i* and *t* specify the particle's index and the iteration number, respectively. *x* and *v* determine the position and velocity of the particle, correspondingly. $r_1$ and $r_2$ are the random values that are generated each time that the equation is used. $c_1$ and $c_2$ are acceleration coefficients, which are often greater than zero and smaller than two [65]. The inertia coefficient of velocity, which is called *w*, is usually between 0.8 and 1.2 [65].

After determining the particle's velocity, the position of the particle is calculated using [64]

$$x_i(t+1) = x_i(t) + v_i(t+1). \tag{41}$$

The PSO algorithm uses an iterative loop whose repetition can be equal to a determined number or based on the finding solution with particular conditions. The detailed algorithm can be found in Ref. [64].

## 7. Results and discussion

The numerical simulation results are next fed to the predictor and optimizer algorithm. Choosing suitable model for estimating target parameters requires taking certain steps. Utilizing *MID*, stated earlier at Section 5, needs that the features are firstly prioritized and then discretized. For instance, five effective elementary features after prioritization for Nusselt number are found to be *Re*, $\lambda_1$, $\phi_2$, *Pr* and $\gamma^*$. The complete ordering of feature prioritization for Nusselt number is shown in Table 6.

Then, to investigate the effect of this prioritization, some models including MLP, support vector regression (SVR) [66], Least Mean Squares algorithm (LMS) [67] and radial basis function (RBF) [68] are tested to estimate Nusselt number, precisely. The result of this experiment is shown in Fig. 3. The mean absolute error (MAE) is used to clearly demonstrate the difference between the calculated and reference values. Considering Fig. 3, MAE shows a decreasing trend if the number of features grows for all the considered models. However, MLP displays a decreasing error and offers the most precise prediction in comparison with the other models, showing why this model is applied in this study. Therefore, a feedforward neural network with one hidden layer is used for MLP.

In addition, to obtain the number of inputs suitable for the model, the effect of increasing the number of model input features on the accuracy of estimating target parameters is calculated. For example, first only the feature *Re*, then two features *Re* and $\lambda_1$ are fed. This is then continued until all features are inputs of the model. According to Fig. 3, four features are sufficient to provide an appropriate MLP model, as the error falls in the minimum value.

The following results were extracted by the estimator algorithm of MLP. It should be pointed out that in the proceedings figures, the default values of the parameters are presented in Table 7, unless the different values are expressed.

It should be pointed out that amongst many variables involved in the current physics, only the most effective parameters were chosen and the results are drawn for them. Fig. 4 shows the variation of Nusselt number versus different values of the effective parameters. It is clear that for $Re = 0$ or stationary flow, by increasing the mixed convection parameter, the Nusselt number raises as a result of intensifying natural convection in comparison with heat conduction. This confirms the powerful impact of natural convection through heat transfer process in the current problem. Similar effect is also found with increases in Reynolds number, which is intensifies the forced convection. Increasing the volume fraction of the nanoparticles can pull up the heat transfer through enhancing conduction in nanofluid. This is more intensive at higher values of mixed convection parameter, which is due to stronger contribution of conduction mechanism to heat transfer at lower Reynolds numbers. Comparing the contribution of these three parameters in heat transfer augmentation throughout the investigated range, volume fraction of nanoparticles is the most influential parameter. In keeping with the literature [27], Fig. 4b shows that reduction in Prandtl number aids the thermal diffusivity and thus cause heat transfer augmentation. As the value of Biot number grows, the temperatures throughout the porous solid and nanofluid approach each other. This is in keeping with the physical expectations, as significant heat exchanges between the solid and fluid phases tend to equalise their temperatures. Under this condition, the local thermal equilibrium assumption is valid and the Nusselt number has slightly improved, rendering increasing heat transfer through solid body. However, it is noted that this simple monotonic trend only exists for relatively low Prandtl numbers ($Pr \le 4$). The physical reason for this convoluted behavior is not immediately obvious but it is certainly related to the competition between the solid and fluid phase in extracting heat from the surface of the cylinder. The thermal conduction of the fluid decreases by increasing Prandtl number and therefore, the solid takes over the fluid by receiving larger heat from the cylinder. Fig. 4b further re-confirms the well-known effect of the permeability of the porous medium upon Nusselt number [20,27,28], in which decreases in permeability parameter results in higher values of Nusselt number. It is to be expected that the fluid can be more penetrating in the solid body and more heat is to be received. Fig. 4c illustrates that enhancing the interfacial area provides more heat transfer surface area and therefore intensifies the heat transfer rate.

In accordance with the classical theory of heat and mass transfer, Fig. 5a shows that Sherwood number enhances with increases in

**Table 7**
Default value of the parameters chosen to draw the figures.

| Parameter | *Re* | $\lambda_1$ | $\phi_2$ | *Pr* | $\gamma^*$ | *D* | $N^*$ | *Df* | *S* | $\lambda$ | $K_c$ | *Bi* | *Sr* | $\gamma$ | *Sc* | $K_s$ |
|---|---|---|---|---|---|---|---|---|---|---|---|---|---|---|---|---|
| Values | 10.0 | 10.0 | 0.1 | 1.0 | 1.0 | 1.0 | 0.1 | 1.0 | 3.7 | 10 | 1.0 | 0.1 | 0.5 | 1.5 | 0.1 | 0.0 |

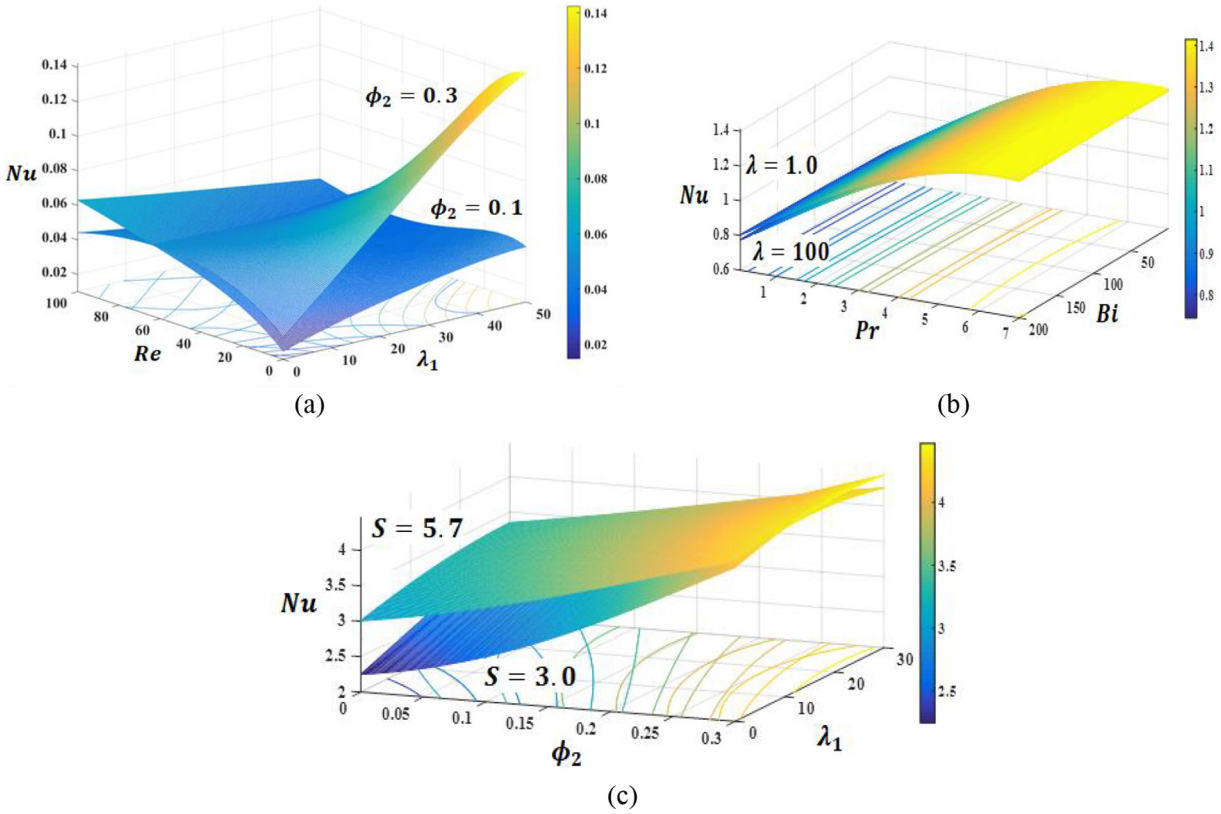


**Fig. 4.** Average Nusselt number for various values of Reynolds number ($Re$), mixed convection parameter ($\lambda_1$), Biot number ($Bi$) and volume fraction of copper nanoparticles ($\phi_2$) at two specified values of (a) copper nanoparticles volume fraction ($\phi_2$), (b) permeability parameter ($\lambda$) and (c) interfacial area ($S$).

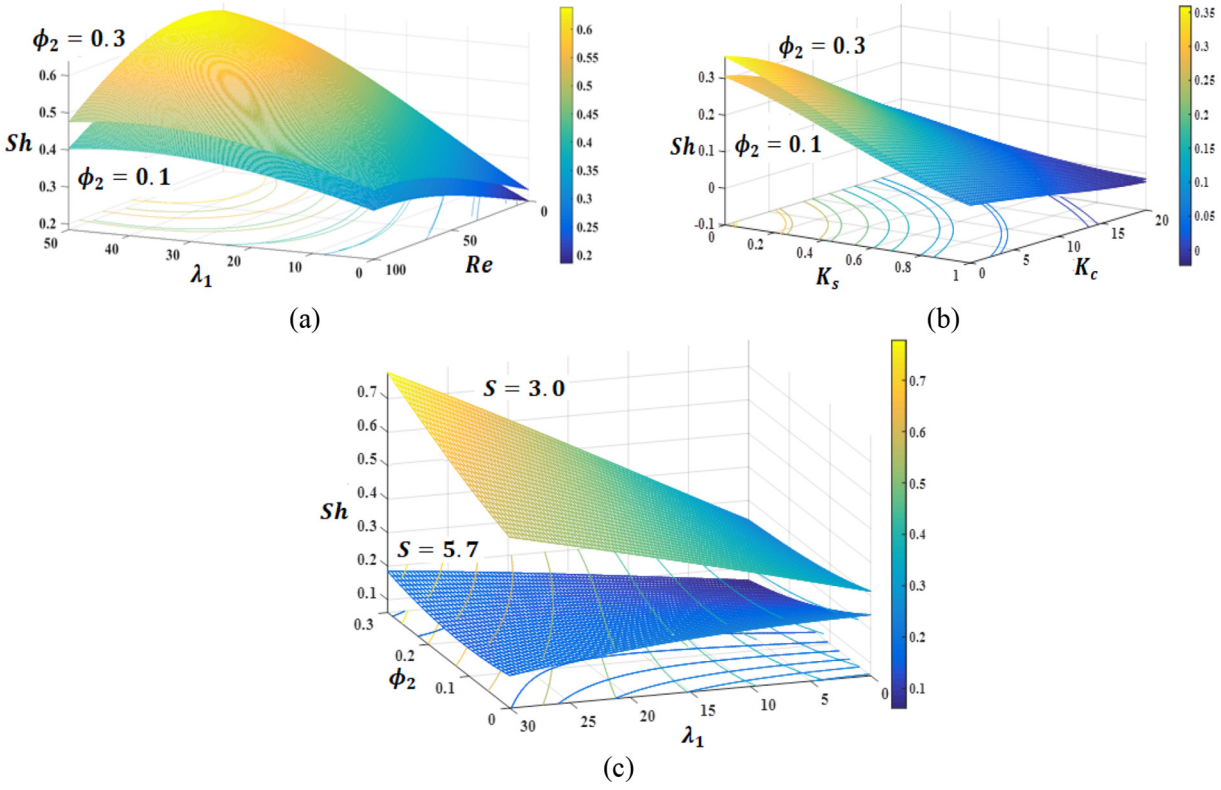


**Fig. 5.** Average Sherwood number for various values of Reynolds number ($Re$), mixed convection parameter ($\lambda_1$), HOM parameter ($K_c$), HET parameter ($K_s$) and volume fraction of copper nanoparticles ($\phi_2$) at two specified values of (a), (b) volume fraction of copper nanoparticles ($\phi_2$) and (c) interfacial area ($S$).

Reynolds number by intensifying convective mass transfer. A similar trend is observed by reducing mixed convection parameter which implies strengthening of forced convection of mass. Increasing the volume fraction of nanoparticles makes the solutal boundary layer thicker through increases in viscosity and thermal conductivity of nanofluid [69]. This results in lower mass transfer at higher volume fraction and low values of Reynolds number where the viscous flow is dominant. However, this is not the case at higher Reynolds number flows in which the flow inertia is being powerful and viscous boundary layer becomes weaker. Fig. 5b depicts that increasing HOM parameter, indicating higher species production through the chemical reaction, renders higher values of Sherwood number. However, increasing HET parameter forms a sharp gradient of species on the cylinder surface (see Eq. (12)). This indicates that mass transfer is dominated by the weaker diffusion mechanism rather than convention transfer. This is the reason for lower mass transfer by the convection process as HET parameter grows. Reducing the interfacial area, allows strengthening of the flow inertia in comparison with viscous layer. This expectedly results in higher mass transfer as Fig. 5c illustrates and has been also confirmed in other studies [70]. All the Sherwood number values in Fig. 5 fall lower than unity, showing that mass diffusion is of greater importance than forced convection of species.

Magnification of Prandtl number intensifies heat transfer from the bluff-body, as stated earlier. This causes a smaller difference between the temperature of the fluid and infinity. That is why the non-dimensional temperature is diminished by increasing Prandtl number in Fig. 6a. This figure also shows that the dimensionless fluid temperature is not sensitive to Biot number. Further, lower non-dimensional permeability parameter, indicating higher permeability of the porous media, facilitates flow convection and this is the reason for existence of more uniform fluid temperature throughout the medium. Nonetheless, a weak dependency of fluid temperature on the permeability is found.

Fig. 6b denotes that by extending the heat exchanging surfaces via increasing $S$, the fluid temperature approaches the values closer to the temperature at infinity as the heat transfer becomes augmented. Variation of dimensionless temperature with respect to increases in $N^*$ indicates a growing trend. This is emanated from involving the same term $T_w - T_\infty$ in the denominator of the non-dimensional parameters of $N^*$and $\theta$. It is expected that the thermal energy received by the flow increases as Dufour number rises. Thus, although Dufour number has no considerable effect on the temperature in this problem, it can potentially enlarge the temperature through the way of developing hot fluid zones. The mixed convection parameter does not have a considerable effect on the temperature, as shown by Fig. 6c. Yet, increasing this parameter may decrease the non-dimensional temperature through shrinkage of the hot fluid zones and spreading them throughout the domain [20,71]. Increasing the volume fraction of nanoparticles from 0.1 to 0.3 results in magnification of non-dimensional temperature. This is inferred from increasing thermal diffusivity, which in turn thickens the thermal boundary layer. Fig. 6d illustrates that further away from the cylinder surface, the fluid non-dimensional temperature approaches zero, matching the boundary condition at the infinity. The temperature rapidly decreases at a small distance from of the cylinder surface, demonstrating a sharp gradient.

Fig. 7a depicts that Biot number variation shows a single-minimum behavior for the non-dimensional temperature of the solid phase of the porous medium. This is followed from the fact that the Biot number is a multi-variable function and its influence on the solid temperature can be complex. At about $Bi = 30$, the solid dimensionless temperature

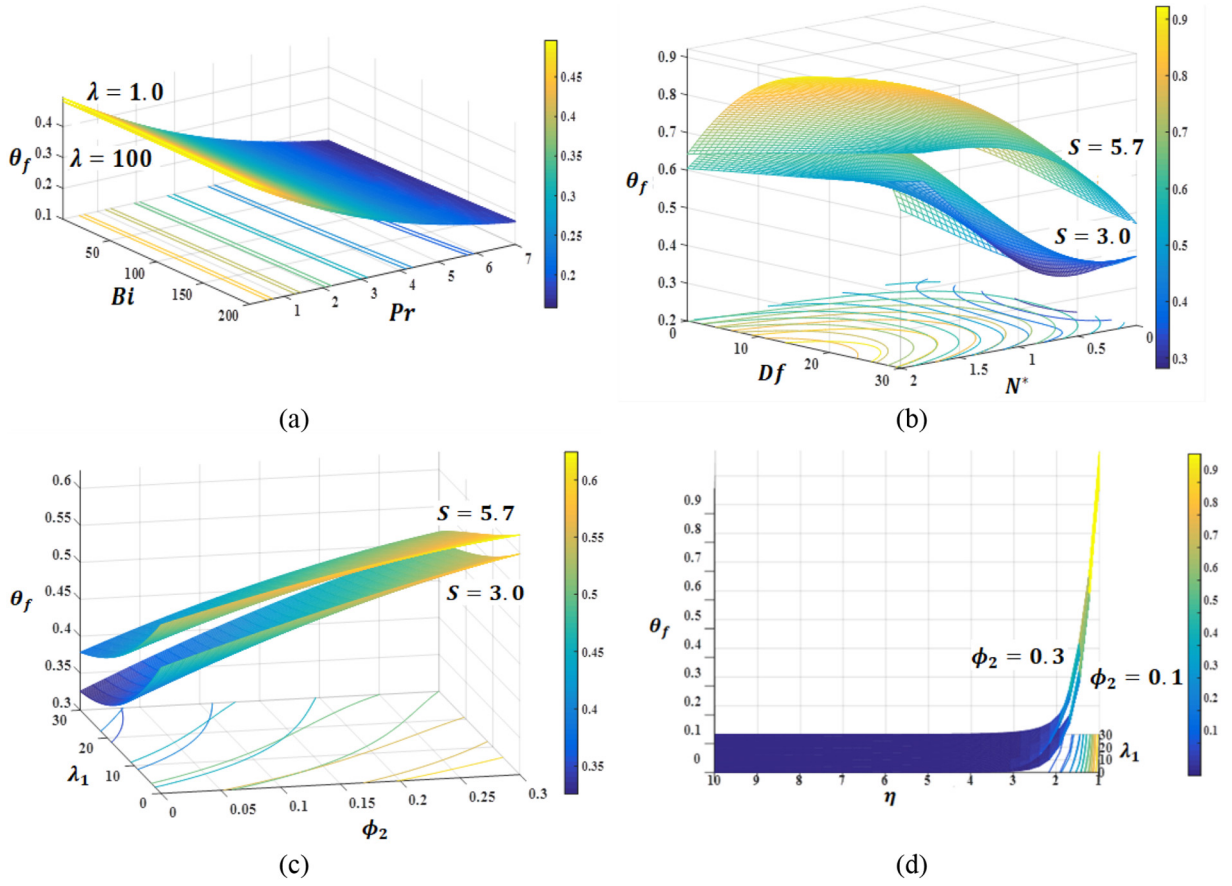


**Fig. 6.** The non-dimensional fluid temperature for various values of Prandtl number ($Pr$), Biot number ($Bi$), Dufour number ($Df$), ratio of concentration to thermal buoyancy forces ($N^*$), mixed convection parameter ($\lambda_1$), copper nanoparticles volume fraction ($\phi_2$), non-dimensional radial distance ($\eta$) at two specified values of (a) permeability parameter ($\lambda$), (b), (c) interfacial area ($S$) and (d) copper nanoparticles volume fraction ($\phi_2$).

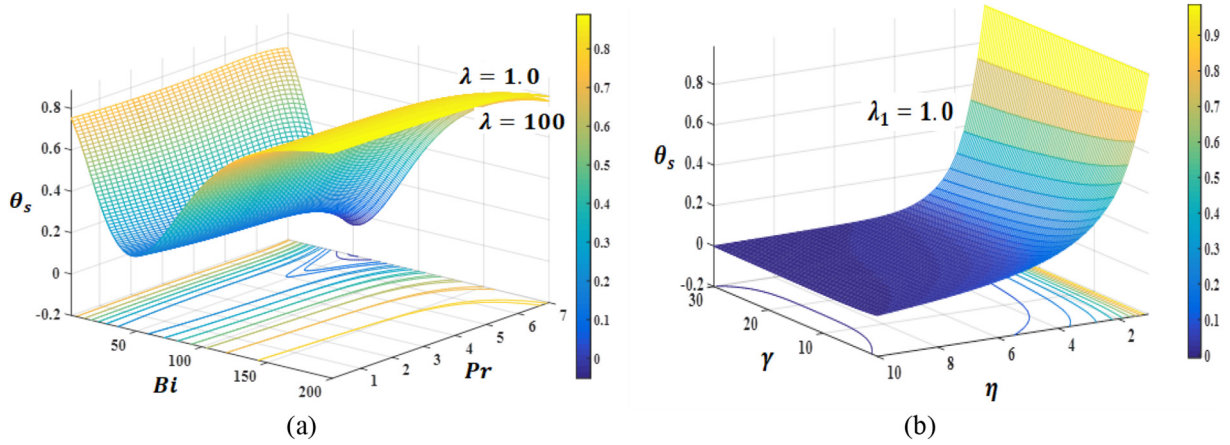


**Fig. 7.** The non-dimensional solid temperature for various values of Prandtl number ($Pr$), Biot number ($Bi$), radial distance ($\eta$) and modified conductivity ratio ($\gamma$) at specified values of (a) permeability parameter ($\lambda$) and (b) mixed convection parameter ($\lambda_1$).

gains the closest value to that at infinity. However, at low or high Biot number, the non-dimensional solid temperature is more intensified, indicating considerable difference between the temperature of body and that of infinity. Both Fig. 7a and b show that the solid temperature is not a strong function of Prandtl number, permeability parameter and modified conductivity ratio. The dimensionless temperature of the solid phase, however, falls down by taking distance from the cylinder surface, such that at $\eta = 4$ the solid temperature approaches that of infinity.

Fig. 8a reveals the strong positive correlation between Reynolds number and concentration of species 1, such that increasing Reynolds number from zero to 100 causes an increment of about 7 times in concentration of $C_1$. Decreasing the mixed convection parameter, implying magnification of Reynolds number, has a similar effect on the concentration of species 1. Intensifying Reynolds number, like rising volume concentration of nanoparticles, allows the heat transfer to be accelerated. As the surface reaction is exothermic, any modification that aids the heat transfer makes the production of species more augmented (see Fig. 8b). This is also obvious from the decreasing concentration of the species 2 versus increasing $\phi_2$ in Fig. 9a. HOM parameter, it does not present considerable impact on the concentration in this figure. Increasing HET parameter of reaction rate diminishes the species production by thickening the solutal boundary layer. Fig. 9a illustrates the opposite trend of Fig. 8 with respect to copper nanoparticles volume fraction and HET parameter, as species 2 is a reactant. The concentration demonstrates no substantial dependency on the Schmidt number (see Fig. 9b). Keeping the diffusivity at a high values, the non-dimensional HET parameter ($K_s = \frac{k_s \upsilon^{1/2}}{D\bar{k}^{1/2}}$) is drastically reduced, such that there is no reaction rate- or $C_2$ consumption, until $D = 15$. Fig. 9b indicates that Soret number, which might be positive or negative [72,73] can affect the recation through manipulating the variation of mass diffusion [20].

One objective of the current study is to estimate the Nusselt and Sherwood number by presenting precise correlations. To do so, similar to what performed for the MLP model, the outputs of numerical simulation were fed to PSO for training the algorithm. Further, according to the prioritization of the features, different proposed equations are evaluated for the Nusselt and Sherwood number estimation. Tables 8 and 9 show respectively the range of chosen parameters in the Nusselt number estimation and the final correlations extracted. The same type of information is presented by Tables 10 and 11 for Sherwood number. In Tables 9 and 11, the proposed correlations become progressively more accurate as more parameters are added to them. This is inferred from mean absolute error (MAE), rendering as a criterion of accuracy of the current predictor correlations against true values of numerical simulation. That is

$$MAE = \frac{\sum_{i=1}^{n} |y_i - x_i|}{n}, \tag{42}$$

where $y_i$ and $x_i$ are respectively the predicted and calculated values and $n$ is the number of points evaluated. The developed correlations can be

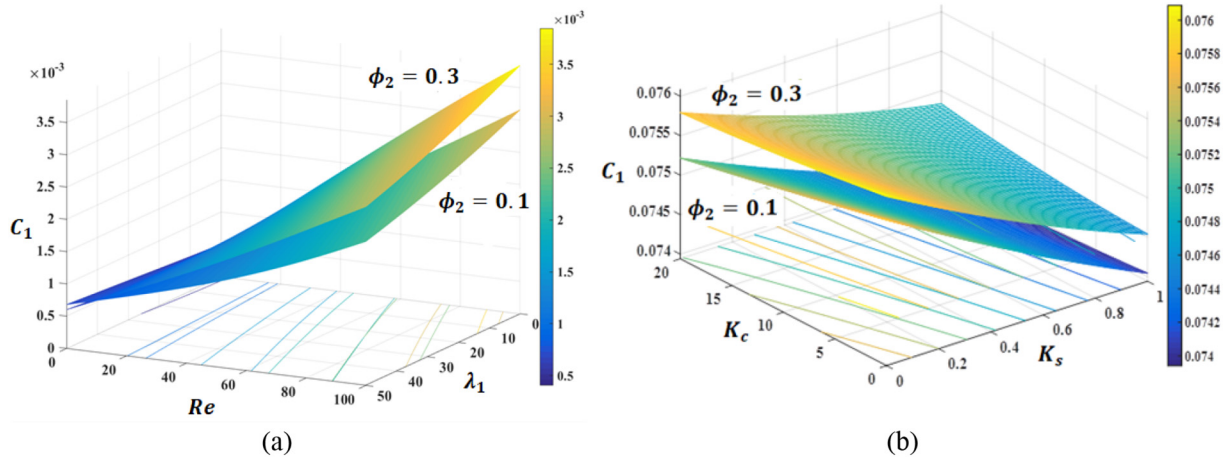


**Fig. 8.** The non-dimensional concentration of species 1 for various values of Reynolds number ($Re$), mixed convection parameter ($\lambda_1$), HOM parameter ($K_c$) and HET parameter ($K_s$) at specified values of (a) and (b) volume fraction of copper nanoparticles ($\phi_2$).

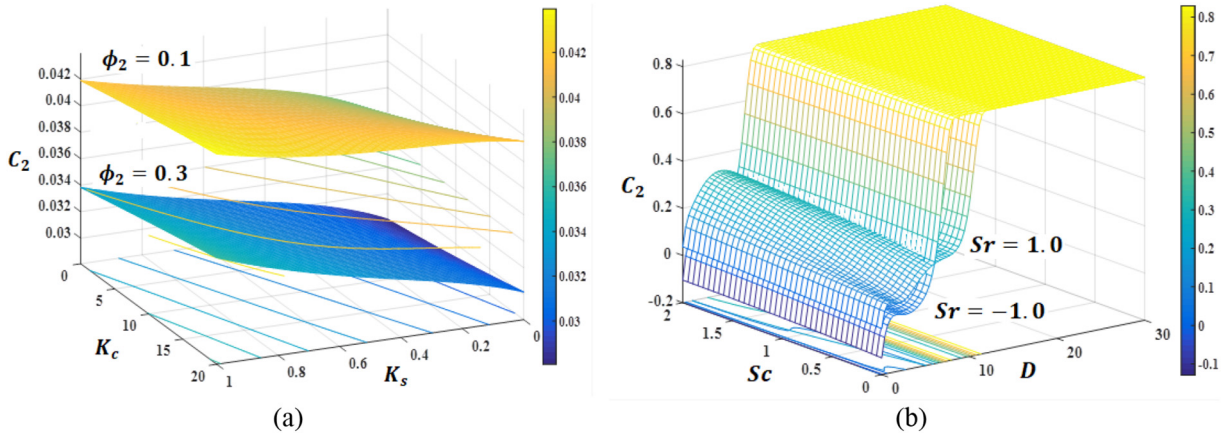


**Fig. 9.** The non-dimensional concentration of species 2 for various values of HOM parameter ($K_c$), HET parameter ($K_s$), diffusion coefficient ($D$) and Schmit number ($Sc$) at specified values of (a) volume fraction of copper nanoparticles ($\phi_2$) and (b) Soret number ($Sr$).

used in other problems that are physically similar to that investigated in this work [74,75].

## 8. Conclusions

A comprehensive analysis of heat and mass transfer in a chemically reacting flow of hybrid nanofluid impinging upon a cylinder embedded in porous media was put forward. The problem included a number of underlying physical and chemical processes including mixed convection, Soret and Dufour effects, homogenous and heterogeneous chemical reactions and local thermal non-equilibrium. Conventional methods for parametric study of such cumbersome problem are computationally quite demanding. More importantly, derivation of correlations for Nusselt and Sherwood numbers would be extremely difficult, if not impossible. This paper, therefore, took a novel approach and employed techniques from artificial intelligence to resolve these issues. A predictor algorithm on the basis of artificial neural network, i.e. multi-layer perception, was applied. This revealed the variations of temperature and concentration fields as well as Nusselt and Sherwood numbers with respect to pertinent parameters. Further, the correlations for Nusselt and Sherwood numbers were presented using particle swarm optimization (PSO) algorithm. It was observed that increasing interfacial area could

**Table 8**
Range of variation for effective parameters involving the Nusselt number correlation.

| | $Re$ | $\lambda_1$ | $\phi_2$ | $Pr$ | $\gamma^*$ |
|---|---|---|---|---|---|
| Effective parameters | $0.1 \le Re \le 150$ | $0.1 \le \lambda_1 \le 50$ | $0 \le \phi_2 \le 0.4$ | $0.1 \le Pr \le 7.0$ | $0 \le \gamma^* \le 7.0$ |

**Table 9**
Nusselt number correlations.

| Nusselt correlation | Effective parameters | Mean absolute error |
|---|---|---|
| $Nu = 1.755 + 0.23 \times Re^{0.636}$ | $Re$ | 0.2770 |
| $Nu = 1.755 + 0.23 \times Re^{0.636} \times {\lambda_1}^{0.146}$ | $Re$, $\lambda_1$ | 0.2560 |
| $Nu = 1.832 + 1.732 \times Re^{0.661} \times {\lambda_1}^{0.156} \times {\phi_2}^{0.938}$ | $Re$, $\lambda_1$, $\phi_2$ | 0.2034 |
| $Nu = 1.832 + 1.732 \times Re^{0.661} \times {\lambda_1}^{0.156} \times {\phi_2}^{0.938} \times Pr^{0.549}$ | $Re$, $\lambda_1$, $\phi_2$, $Pr$ | 0.1568 |
| $Nu = 1.832 + 1.732 \times Re^{0.661} \times {\lambda_1}^{0.156} \times {\phi_2}^{0.938} \times Pr^{0.549} \times {\gamma^*}^{8.642}$ | $Re$, $\lambda_1$, $\phi_2$, Pr , $\gamma^*$ | 0.1421 |

**Table 10**
Range of variation for effective parameters involving the Sherwood number correlation.

| | $Sc$ | $\gamma^*$ | $\lambda_1$ | $D$ | $Sr$ | $N^*$ |
|---|---|---|---|---|---|---|
| Effective parameters | $0.1 \le Sc \le 3.0$ | $0 \le \gamma^* \le 7.0$ | $0.1 \le \lambda_1 \le 50$ | $0.1 \le D \le 30$ | $-1.0 \le Sr \le 1.0$ | $0 \le N^* \le 2.0$ |

**Table 11**
Sherwood number correlations.

| Sherwood correlation | Effective parameters | Mean absolute error |
|---|---|---|
| $Sh = 0.027 + 0.604 \times Sc^{0.385}$ | $Sc$ | 0.1229 |
| $Sh = 0.099 + 0.512 \times Sc^{0.462} \times {\gamma^*}^{1.031}$ | $Sc$, $\gamma^*$ | 0.0932 |
| $Sh = 0.099 + 0.512 \times Sc^{0.462} \times {\gamma^*}^{1.031} \times {\lambda_1}^{0.257}$ | $Sc$, $\gamma^*$, $\lambda_1$, | 0.0854 |
| $Sh = 0.141 + 0.454 \times Sc^{0.525} \times {\gamma^*}^{1.159} \times {\lambda_1}^{0.305} \times D^{0.269}$ | $Sc$, $\gamma^*$, $\lambda_1$, $D$ | 0.0789 |
| $Sh = 0.221 + 0.637 \times Sc^{0.759} \times {\gamma^*}^{1.617} \times {\lambda_1}^{0.500} \times D^{0.479} \times Sr^{1.011}$ | $Sc$, $\gamma^*$, $\lambda_1$, $D$, $Sr$ | 0.0734 |
| $Sh = 0.242 + 0.547 \times Sc^{0.893} \times {\gamma^*}^{1.876} \times {\lambda_1}^{0.621} \times D^{0.619} \times Sr^{1.045} \times {N^*}^{1.552}$ | $Sc$, $\gamma^*$, $\lambda_1$, $D$, $Sr$, $N^*$ | 0.0677 |

enhance heat transfer and non-dimensional temperature, while it weakened mass transfer. Decreasing mixed convection parameter, or increasing Reynolds number, promoted heat transfer and dimensionless fluid temperature. However, it had a negligible effect on the temperature of the solid phase. Although reducing permeability lead to intensification of heat and mass transfer, solid temperature had little dependency upon that. Volume fraction of nanoparticles was shown to be an influential parameter on the heat transfer and species production. HOM parameter appeared to be ineffective on the species concentration. Yet, HET parameter presented a strong contribution to species consumption and production. The importance of Soret effect on the species concentration was modified by magnification of diffusivity. As an important outcome, correlations for Nusselt and Sherwood numbers were developed systematically through a progressive increase in the number of considered parameters. A high level of accuracy was reported for correlations that involve more than five parameters. This study clearly demonstrated the potentials of artificial intelligence in tackling complicated problems in thermo-chemical and solutal systems that are not amenable to conventional methods of analysis. Future studies may concentrate on more complicated configurations or addition of further details to the chemistry and transport phenomena.

## CRediT authorship contribution statement

**Javad Mohebbi Najm Abad:** Data curation, Formal analysis, Investigation. **Rasool Alizadeh:** Formal analysis, Validation. **Abolfazl Fattahi:** Writing - review & editing. **Mohammad Hossein Doranehgard:** Software. **Ebrahim Alhajri:** Software. **Nader Karimi:** Conceptualization, Supervision, Writing - review & editing.

## Declaration of competing interest

The authors declare that they have no known competing financial interests or personal relationships that could have appeared to influence the work reported in this paper.

## Acknowledgment

N. Karimi acknowledges the financial support of Engineering and Physical Science Research Council through grant EP/N020472/1.

## References

[1] A.A. Nassani, A.M. Aldakhil, M.M.Q. Abro, K. Zaman, A. Kabbani, Resource management for green growth: ensure environment sustainability agenda for mutual exclusive global gain, Environ. Prog. Sustain. Energy 38 (4) (2019), 13132.
[2] J.R. Vázquez-Canteli, S. Ulyanin, J. Kämpf, Z. Nagy, Fusing TensorFlow with building energy simulation for intelligent energy management in smart cities, Sustain. Cities Soc. 45 (2019) 243–257.
[3] A.M. Abdulateef, S. Mat, J. Abdulateef, K. Sopian, A.A. Al-Abidi, Geometric and design parameters of fins employed for enhancing thermal energy storage systems: a review, Renew. Sust. Energ. Rev. 82 (2018) 1620–1635.
[4] G.K. Chhaparwal, A. Srivastava, R. Dayal, Artificial repeated-rib roughness in a solar air heater–a review, Sol. Energy 194 (2019) 329–359.
[5] T. Alam, R.P. Saini, J.S. Saini, Heat and flow characteristics of air heater ducts provided with turbulators—a review, Renew. Sust. Energ. Rev. 31 (2014) 289–304.
[6] S.U. Choi, J.A. Eastman, Enhancing Thermal Conductivity of Fluids With Nanoparticles (No. ANL/MSD/CP-84938; CONF-951135-29), Argonne National Lab, IL (United States), 1995.
[7] M.H. Esfe, S. Esfandeh, M.K. Amiri, M. Afrand, A novel applicable experimental study on the thermal behavior of SWCNTs (60%)-MgO (40%)/EG hybrid nanofluid by focusing on the thermal conductivity, Powder Technol. 342 (2019) 998–1007.
[8] M. Afrand, Experimental study on thermal conductivity of ethylene glycol containing hybrid nano-additives and development of a new correlation, Appl. Therm. Eng. 110 (2017) 1111–1119.
[9] W. Yu, D.M. France, J.L. Routbort, S.U. Choi, Review and comparison of nanofluid thermal conductivity and heat transfer enhancements, Heat transfer engineering 29 (5) (2008) 432–460.
[10] C. Kleinstreuer, Y. Feng, Experimental and theoretical studies of nanofluid thermal conductivity enhancement: a review, Nanoscale Res. Lett. 6 (1) (2011) 229.
[11] M. Akbarzadeh, S. Rashidi, N. Karimi, N. Omar, First and second laws of thermodynamics analysis of nanofluid flow inside a heat exchanger duct with wavy walls and a porous insert, J. Therm. Anal. Calorim. 135 (1) (2019) 177–194.
[12] D.G. Guthrie, M. Torabi, N. Karimi, Combined heat and mass transfer analyses in catalytic microreactors partially filled with porous material-the influences of nanofluid and different porous-fluid interface models, Int. J. Therm. Sci. 140 (2019) 96–113.
[13] D.G. Guthrie, M. Torabi, N. Karimi, Energetic and entropic analyses of double-diffusive, forced convection heat and mass transfer in microreactors assisted with nanofluid, J. Therm. Anal. Calorim. 137 (2) (2019) 637–658.
[14] M. Torabi, C. Dickson, N. Karimi, Theoretical investigation of entropy generation and heat transfer by forced convection of copper–water nanofluid in a porous channel—local thermal non-equilibrium and partial filling effects, Powder Technol. 301 (2016) 234–254.
[15] Q. Xiong, I. Tlili, J.A. Ali, S.M. Hamad, A. Shafee, T. Nguyen-Thoi, H. Hamouda, Modeling of hybrid nanofluid behavior within a permeable media involving buoyancy effect, Physica A: Statistical Mechanics and its Applications (2019) 123940.
[16] S.A. Mehryan, F.M. Kashkooli, M. Ghalambaz, A.J. Chamkha, Free convection of hybrid $Al_2O_3$-Cu water nanofluid in a differentially heated porous cavity, Adv. Powder Technol. 28 (9) (2017) 2295–2305.
[17] H. Sajjadi, A.A. Delouei, M. Izadi, R. Mohebbi, Investigation of MHD natural convection in a porous media by double MRT lattice Boltzmann method utilizing MWCNT–$Fe_3O_4$/water hybrid nanofluid, Int. J. Heat Mass Transf. 132 (2019) 1087–1104.
[18] T.D. Manh, N.D. Nam, G.K. Abdulrahman, M.H. Khan, I. Tlili, A. Shafee, M. Shamlooei, T. Nguyen-Thoi, Investigation of hybrid nanofluid migration within a porous closed domain, Physica A: Statistical Mechanics and its Applications (2019) 123960.
[19] S.A.M. Mehryan, M.A. Sheremet, M. Soltani, M. Izadi, Natural convection of magnetic hybrid nanofluid inside a double-porous medium using two-equation energy model, J. Mol. Liq. 277 (2019) 959–970.
[20] R. Alizadeh, N. Karimi, A. Mehdizadeh, A. Nourbakhsh, Analysis of transport from cylindrical surfaces subject to catalytic reactions and non-uniform impinging flows in porous media, J. Therm. Anal. Calorim. 138 (1) (2019) 659–678.
[21] A. Jarray, Z. Mehrez, A. El Cafsi, Mixed convection Ag-MgO/water hybrid nanofluid flow in a porous horizontal channel, The European Physical Journal Special Topics 228 (12) (2019) 2677–2693.
[22] E. Aminian, H. Moghadasi, H. Saffari, Magnetic field effects on forced convection flow of a hybrid nanofluid in a cylinder filled with porous media: a numerical study, J. Therm. Anal. Calorim. (2020) 1–13.
[23] N. Abbas, M.Y. Malik, S. Nadeem, Study of three dimensional stagnation point flow of hybrid nanofluid over an isotropic slip surface, Physica A: Statistical Mechanics and its Applications (2020), 124020. https://doi.org/10.1016/j.physa.2019.124020.
[24] D. Pal, G. Mandal, Mixed convection–radiation on stagnation-point flow of nanofluids over a stretching/shrinking sheet in a porous medium with heat generation and viscous dissipation, J. Pet. Sci. Eng. 126 (2015) 16–25.
[25] F.M. Ali, R. Nazar, N.M. Arifin, I. Pop, MHD stagnation-point flow and heat transfer towards stretching sheet with induced magnetic field, Appl. Math. Mech. 32 (4) (2011) 409–418.
[26] F. Mabood, W.A. Khan, Approximate analytic solutions for influence of heat transfer on MHD stagnation point flow in porous medium, Comput. Fluids 100 (2014) 72–78.
[27] R. Alizadeh, A.B. Rahimi, N. Karimi, A. Alizadeh, On the hydrodynamics and heat convection of an impinging external flow upon a cylinder with transpiration and embedded in a porous medium, Transp. Porous Media 120 (3) (2017) 579–604.
[28] R. Alizadeh, N. Karimi, R. Arjmandzadeh, A. Mehdizadeh, Mixed convection and thermodynamic irreversibilities in MHD nanofluid stagnation-point flows over a cylinder embedded in porous media, J. Therm. Anal. Calorim. 135 (1) (2019) 489–506.
[29] N.S. Khashi'ie, N.M. Arifin, R. Nazar, E.H. Hafidzuddin, N. Wahi, I. Pop, Magnetohydrodynamics (MHD) axisymmetric flow and heat transfer of a hybrid nanofluid past a radially permeable stretching/shrinking sheet with joule heating, Chin. J. Phys. 64 (2020) 251–263.
[30] S.B. Hacene, F. Ghomari, F. Schoefs, A. Khelidj, Probabilistic modelling of compressive strength of concrete using response surface methodology and neural networks, Arab. J. Sci. Eng. 39 (6) (2014) 4451–4460.
[31] M. Mohanraj, S. Jayaraj, C. Muraleedharan, Applications of artificial neural networks for thermal analysis of heat exchangers–a review, Int. J. Therm. Sci. 90 (2015) 150–172.
[32] A. Abdollahi, M. Shams, A. Abdollahi, Artificial neural network modeling of a deflector in a grooved channel as well as optimization of its effective parameters, Heat Mass Transf. 54 (1) (2018) 59–68.
[33] A. Abdollahi, M. Shams, Optimization of heat transfer enhancement of nanofluid in a channel with winglet vortex generator, Appl. Therm. Eng. 91 (2015) 1116–1126.
[34] C. Uysal, M.E. Korkmaz, Estimation of entropy generation for Ag-MgO/water hybrid nanofluid flow through rectangular minichannel by using artificial neural network, Politeknik Dergisi 22 (1) (2019) 41–51.
[35] H. Bagheri, M. Behrang, E. Assareh, M. Izadi, M.A. Sheremet, Free convection of hybrid nanofluids in a C-shaped chamber under variable heat flux and magnetic field: simulation, sensitivity analysis, and artificial neural networks, Energies 12 (14) (2019) 2807.
[36] Q. Xiong, M. Ayani, A.A. Barzinjy, R.N. Dara, A. Shafee, T. Nguyen-Thoi, Modeling of heat transfer augmentation due to complex-shaped turbulator using nanofluid, Physica A: Statistical Mechanics and Its Applications 540 (2020), 122465.
[37] A. Izadi, M. Siavashi, H. Rasam, Q. Xiong, MHD enhanced nanofluid mediated heat transfer in porous metal for CPU cooling, Appl. Therm. Eng. 168 (2020), 114843.
[38] M. Sadeghzadeh, H. Maddah, M.H. Ahmadi, A. Khadang, M. Ghazvini, A. Mosavi, N. Nabipour, Prediction of thermo-physical properties of $TiO_2$-$Al_2O_3$/water nanoparticles by using artificial neural network, Nanomaterials 10 (4) (2020) 697.

[39] F. Nasirzadehroshenin, M. Sadeghzadeh, A. Khadang, H. Maddah, M.H. Ahmadi, H. Sakhaeinia, L. Chen, Modeling of heat transfer performance of carbon nanotube nanofluid in a tube with fixed wall temperature by using ANN–GA, The European Physical Journal Plus 135 (2) (2020) 1–20.
[40] M.H. Ahmadi, B. Mohseni-Gharyehsafa, M. Farzaneh-Gord, R.D. Jilte, R. Kumar, K.W. Chau, Applicability of connectionist methods to predict dynamic viscosity of silver/water nanofluid by using ANN-MLP, MARS and MPR algorithms, Engineering Applications of Computational Fluid Mechanics 13 (1) (2019) 220–228.
[41] A. Baghban, A. Jalali, M. Shafiee, M.H. Ahmadi, K.W. Chau, Developing an ANFIS-based swarm concept model for estimating the relative viscosity of nanofluids, Engineering Applications of Computational Fluid Mechanics 13 (1) (2019) 26–39.
[42] G. Hunt, N. Karimi, M. Torabi, Two-dimensional analytical investigation of coupled heat and mass transfer and entropy generation in a porous, catalytic microreactor, Int. J. Heat Mass Transf. 119 (2018) 372–391.
[43] G.F. Al-Sumaily, H.M. Hussen, M.C. Thompson, Validation of thermal equilibrium assumption in free convection flow over a cylinder embedded in a packed bed, International Communications in Heat and Mass Transfer 58 (2014) 184–192.
[44] C. Liu, M. Pan, L. Zheng, P. Lin, Effects of heterogeneous catalysis in porous media on nanofluid-based reactions, International Communications in Heat and Mass Transfer 110 (2020), 104434.
[45] T. Hayat, M. Mustafa, S. Mesloub, Mixed convection boundary layer flow over a stretching surface filled with a Maxwell fluid in presence of Soret and Dufour effects, Zeitschrift für Naturforschung A 65 (5) (2010) 401–410.
[46] N. Freidoonimehr, M.M. Rashidi, S. Abelman, G. Lorenzini, Analytical modeling of MHD flow over a permeable rotating disk in the presence of Soret and Dufour effects: entropy analysis, Entropy 18 (5) (2016) 131.
[47] C.G. Hill, T.W. Root, An Introduction to Chemical Engineering Kinetics & Reactor Design, Wiley, New York, 1977 245–316.
[48] J. Ahmed, M. Khan, L. Ahmad, Stagnation point flow of Maxwell nanofluid over a permeable rotating disk with heat source/sink, J. Mol. Liq. 287 (2019), 110853.
[49] R. Alizadeh, A.B. Rahimi, R. Arjmandzadeh, M. Najafi, A. Alizadeh, Unaxisymmetric stagnation-point flow and heat transfer of a viscous fluid with variable viscosity on a cylinder in constant heat flux, Alexandria Engineering Journal 55 (2) (2016) 1271–1283.
[50] R. Alizadeh, A.B. Rahimi, M. Najafi, Unaxisymmetric stagnation-point flow and heat transfer of a viscous fluid on a moving cylinder with time-dependent axial velocity, J. Braz. Soc. Mech. Sci. Eng. 38 (1) (2016) 85–98.
[51] Q. Xiong, M. Vaseghi, J.A. Ali, S.M. Hamad, M. Jafaryar, M. Sheikholeslami, Z. Li, Nanoparticle application for heat transfer and irreversibility analysis in an air conditioning unit, J. Mol. Liq. 292 (2019), 111372.
[52] Q. Xiong, E. Abohamzeh, J.A. Ali, S.M. Hamad, I. Tlili, A. Shafee, T.K. Nguyen, Influences of nanoparticles with various shapes on MHD flow inside wavy porous space in appearance of radiation, J. Mol. Liq. 292 (2019), 111386.
[53] Q. Xiong, M. Jafaryar, A. Divsalar, M. Sheikholeslami, A. Shafee, D.D. Vo, Z. Li, Macroscopic simulation of nanofluid turbulent flow due to compound turbulator in a pipe, Chem. Phys. 527 (2019), 110475.
[54] S.S. Ghadikolaei, M. Yassari, H. Sadeghi, K. Hosseinzadeh, D.D. Ganji, Investigation on thermophysical properties of $Tio_2$–Cu/$H_2O$ hybrid nanofluid transport dependent on shape factor in MHD stagnation point flow, Powder Technol. 322 (2017) 428–438.
[55] T.L. Bergman, F.P. Incropera, A.S. Lavine, D.P. DeWitt, Introduction to Heat Transfer, John Wiley & Sons, 2011.
[56] C.Y. Wang, Axisymmetric stagnation flow on a cylinder, Q. Appl. Math. 32 (2) (1974) 207–213.
[57] R.S.R. Gorla, Heat transfer in an axisymmetric stagnation flow on a cylinder, Appl. Sci. Res. 32 (5) (1976) 541–553.
[58] M. Hamid, T. Zubair, M. Usman, Z.H. Khan, W. Wang, Natural convection effects on heat and mass transfer of slip flow of time-dependent Prandtl fluid, Journal of Computational Design and Engineering 6 (4) (2019) 584–592.
[59] M.H. Hassoun, Fundamentals of Artificial Neural Networks, MIT press, 1995.
[60] A.Y. Alanis, N. Arana-Daniel, C. Lopez-Franco, Artificial Neural Networks for Engineering Applications, Academic Press, 2019.
[61] N. AlNuaimi, M.M. Masud, M.A. Serhani, N. Zaki, Streaming feature selection algorithms for big data: a survey, Applied Computing and Informatics (2019)https://doi.org/10.1016/j.aci.2019.01.001.
[62] C.O. Sakar, O. Kursun, F. Gurgen, A feature selection method based on kernel canonical correlation analysis and the minimum Redundancy–Maximum Relevance filter method, Expert Syst. Appl. 39 (3) (2012) 3432–3437.
[63] K.E. Parsopoulos, M.N. Vrahatis, Particle Swarm Optimization and Intelligence: Advances and Applications, 2010.
[64] T.V. Sibalija, Particle swarm optimisation in designing parameters of manufacturing processes: a review (2008–2018), Appl. Soft Comput. 84 (2019), 105743.
[65] F. Chan, M. Tiwari, Swarm Intelligence: Focus on Ant and Particle Swarm Optimization, BoD–Books on Demand, 2007.
[66] H. Drucker, C.J. Burges, L. Kaufman, A.J. Smola, V. Vapnik, Support vector regression machines, Adv Neural Inf Process Syst (1997) 155–161.
[67] T. Strutz, Data Fitting and Uncertainty. A Practical Introduction to Weighted Least Squares and Beyond, Vieweg+ Teubner, 2010.
[68] D.S. Broomhead, D. Lowe, Radial Basis Functions, Multi-variable Functional Interpolation and Adaptive Networks (No. RSRE-MEMO-4148), Royal Signals and Radar Establishment Malvern, United Kingdom, 1988.
[69] R. Chowdhury, S. Parvin, M.A.H. Khan, Finite element analysis of double-diffusive natural convection in a porous triangular enclosure filled with $Al_2O_3$-water nanofluid in presence of heat generation, Heliyon 2 (8) (2016), e00140.
[70] J. Cho, M.D. Annable, P.S.C. Rao, Measured mass transfer coefficients in porous media using specific interfacial area, Environmental science & technology 39 (20) (2005) 7883–7888.
[71] A. Hamid, M. Alghamdi, M. Khan, A.S. Alshomrani, An investigation of thermal and solutal stratification effects on mixed convection flow and heat transfer of Williamson nanofluid, J. Mol. Liq. 284 (2019) 307–315.
[72] G. Hunt, N. Karimi, B. Yadollahi, M. Torabi, The effects of exothermic catalytic reactions upon combined transport of heat and mass in porous microreactors, Int. J. Heat Mass Transf. 134 (2019) 1227–1249.
[73] C. Dickson, M. Torabi, N. Karimi, First and second law analysis of nanofluid convection through a porous channel-the effects of partial filling and internal heat sources, J. Appl. Therm. Eng. 103 (2016) 459–480.
[74] R. Razavi, A. Sabaghmoghadam, A. Bemani, A. Baghban, K.W. Chau, E. Salwana, Application of ANFIS and LSSVM strategies for estimating thermal conductivity enhancement of metal and metal oxide based nanofluids, Engineering Applications of Computational Fluid Mechanics 13 (1) (2019) 560–578.
[75] M.H. Ahmadi, M. Sadeghzadeh, H. Maddah, A. Solouk, R. Kumar, K.W. Chau, Precise smart model for estimating dynamic viscosity of $SiO_2$/ethylene glycol–water nanofluid, Engineering Applications of Computational Fluid Mechanics 13 (1) (2019) 1095–1105.